



Fast continuous measurement of synchrotron powder diffraction synchronized with controlling gas and vapour pressures at beamline BL02B2 of SPring-8

Shogo Kawaguchi,^{a,*} Michitaka Takemoto,^b Hideki Tanaka,^c Shotaro Hiraide,^d Kunihisa Sugimoto^{a,e} and Yoshiki Kubota^f

Received 11 November 2019

Accepted 4 February 2020

Edited by A. F. Craievich, University of São Paulo, Brazil

Keywords: X-ray powder diffraction; *in situ* measurements; time resolved; gas adsorption/desorption; beamlines.

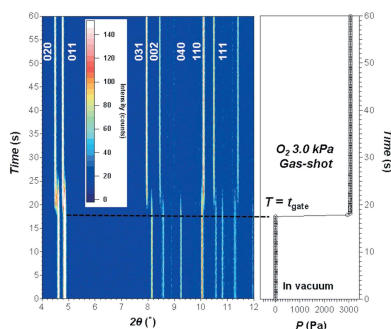
^aDiffraction and Scattering Division, Japan Synchrotron Radiation Research Institute (JASRI), 1-1-1 Kouto, Sayo-cho, Sayo-gun, Hyogo 679-5198, Japan, ^bEngineering Support Group, Japan Synchrotron Radiation Research Institute (JASRI), 1-1-1 Kouto, Sayo-cho, Sayo-gun, Hyogo 679-5198, Japan, ^cResearch Initiative for Supra-Materials (RISM), Shinshu University, 4-17-1 Wakasato, Nagano 380-8553, Japan, ^dDepartment of Chemical Engineering, Kyoto University, Nishikyo, Kyoto 615-8510, Japan, ^eInstitute for Integrated Cell-Material Sciences, Kyoto University Institute for Advanced Study, Kyoto University, Yoshida Ushinomiya-cho, Sakyo-ku, Kyoto 606-8501, Japan, and ^fDepartment of Physical Science, Osaka Prefecture University, Osaka 599-8531, Japan. *Correspondence e-mail: kawaguchi@spring8.or.jp

A gas- and vapour-pressure control system synchronized with the continuous data acquisition of millisecond high-resolution powder diffraction measurements was developed to study structural change processes in gas storage and reaction materials such as metal organic framework compounds, zeolite and layered double hydroxide. The apparatus, which can be set up on beamline BL02B2 at SPring-8, mainly comprises a pressure control system of gases and vapour, a gas cell for a capillary sample, and six one-dimensional solid-state (MYTHEN) detectors. The pressure control system can be remotely controlled via developed software connected to a diffraction measurement system and can be operated in the closed gas and vapour line system. By using the temperature-control system on the sample, high-resolution powder diffraction data can be obtained under gas and vapour pressures ranging from 1 Pa to 130 kPa in temperatures ranging from 30 to 1473 K. This system enables one to perform automatic and high-throughput *in situ* X-ray powder diffraction experiments even at extremely low pressures. Furthermore, this developed system is useful for studying crystal structures during the adsorption/desorption processes, as acquired by millisecond and continuous powder diffraction measurements. The acquisition of diffraction data can be synchronized with the control of the pressure with a high frame rate of up to 100 Hz. *In situ* and time-resolved powder diffraction measurements are demonstrated for nanoporous Cu coordination polymer in various gas and vapour atmospheres.

1. Introduction

X-ray powder diffraction (XRPD) is a well established technique for phase identification and the determination of the atomic structure of crystalline materials. Synchrotron XRPD provides high angular and spatial resolution data in a short time. The angular resolution reaches the order of 0.001° in 2θ and the observable Q range is over 30 \AA^{-1} when using high-energy X-rays. These data provide us with useful and varied information for the advancement of material science. Therefore, powder diffraction beamlines currently exist in synchrotron radiation facilities worldwide and the high-throughput data collection of XRPD can be performed by a robotic sample changer (Wang *et al.*, 2008; Thompson *et al.*, 2009; Kawaguchi *et al.*, 2017).

XRPD experiments under non-ambient conditions (*e.g.* temperature, pressure, electric field, gas atmosphere and



electrochemical reaction) are frequently performed owing to the increasing demand for the investigation of functional materials *in operando*. In particular, *in situ* powder diffraction experiments under a gas atmosphere are one of the most powerful tools used to investigate the crystal structure of gas storage/separation materials. Such crystallographic studies have been actively performed since the emergence of third-generation synchrotron radiation facilities. XRPD measurements of the transmission geometry by using a capillary became a prevalent method owing to the high-energy X-rays from the synchrotron radiation. Therefore, we can easily control the sample environment for a small amount of powder sample by using various gas cells for the capillary sample (Brunelli & Fitch, 2003; Jensen *et al.*, 2010; Hill, 2013). Various materials have been investigated through *in situ* XRPD experiments [*e.g.* metal organic framework (MOF) compounds (Kubota *et al.*, 2007; Carrington *et al.*, 2014), zeolite (Norby, 1997; Cho *et al.*, 2012) and hydrogen-storage alloys (Dekura *et al.*, 2018)]. Most studies conducted the crystal structure analysis under static conditions along the premeasurement results of isothermal adsorption curves. This measurement is crucial for characterizing the material function for the applications of gas storage, separation and so on. Observations of continuous structural changes under gas adsorption and desorption processes are also important for understanding the overall material functions to improve thermodynamic and kinetic gas separation properties, and storage capacity. However, such an experimental diffraction method is not common even now and the continuous collection of XRPD patterns with wide 2θ ranges must be done as fast as possible. Recently, hybrid photon-counting X-ray detectors have been improved and XRPD patterns can now be collected with a temporal resolution of milliseconds. In particular, the one-dimensional Si micro-strip MYTHEN detector (Schmitt *et al.*, 2003) has been widely used at XRPD beamlines (Haverkamp & Wallwork, 2009; Bergamaschi *et al.*, 2010; Thompson *et al.*, 2011), and we can collect time-resolved data with high angular resolutions, opening up new perspectives for *in situ* XRPD. To fully utilize the detectors and promote further materials science, an apparatus is required that can control the sample environment synchronized with the XRPD data on the order of milliseconds.

Herein, we report a new gas- and vapour-pressure control system synchronized with continuous high-resolution XRPD measurements. The apparatus, which was set up on beamline BL02B2 at SPring-8 in Japan (Kawaguchi *et al.*, 2017), mainly comprises a pressure control system for gas and vapour, a gas cell for the capillary sample, and multiple MYTHEN detectors. The pressure control system can be controlled remotely via developed software connected to an XRPD system. This developed system can control the gas atmosphere automatically as effectively as the previous study (Hill, 2013), while also measuring the time-resolved XRPD data with a temporal resolution of milliseconds under the adsorption/desorption processes. By using the developed apparatus, we demonstrate automatic *in situ* XRPD experiments under gas and vapour pressures and time-resolved high-resolution

XRPD measurements under the gas adsorption processes for a MOF sample.

2. Experiment and development of apparatus

2.1. Powder diffraction beamline BL02B2 at SPring-8

In the powder diffraction station for the bending-magnet source beamline BL02B2 at the third-generation synchrotron facility SPring-8, the beamline is specialized for high-resolution XRPD on crystalline materials and it provides X-ray energies of 12–37 keV with a resolution of $\Delta E/E \simeq 2 \times 10^{-4}$. In the optics hutch, an Si mirror coated with Ni and Pt is located in front of the Si (111) double-crystal monochromator. This mirror can eliminate the higher harmonics of X-rays. After the monochromatization of X-rays, a horizontal beam with a width of 10 mm is focused using a sagittal cylindrical mirror coated with Pt. The beam dimensions at the sample position are generally 0.5 mm \times 1.5 mm (V \times H). In the experimental hutch, a two-circle powder diffractometer equipped with six one-dimensional MYTHEN detectors and an imaging plate detector was installed. The detector setup was presented in a previous report (Kawaguchi *et al.*, 2017) and two types of scan mode using the MYTHEN detectors are available. One of the modes acquires data at differential 2θ positions, and this scan provides a large 2θ range up to 80° . This mode is useful for examining the crystal structure under static conditions. The other mode records the diffraction data simultaneously at 2θ values ranging from 2 to 38° . In the single-shot measurement, the detector gaps between modules in the positive 2θ region can be covered by those in the negative 2θ region. This setup is suitable for *in situ* and/or time-resolved measurements. The sample temperature can be changed by He/N₂ gas flow and hot N₂ gas flow devices, and the temperature range of 30–1100 K can be controlled. In this study, all experiments were conducted using MYTHEN detectors and an X-ray energy of 15.5 keV. All of the development and measurements were conducted at beamline BL02B2 of SPring-8.

2.2. Development of gas-handling system

We developed a remote gas- and vapour-pressure control (RGVPC) system for *in situ* XRPD measurements under gas and vapour atmospheres. The RGVPC system mainly consists of a gas-pressure control unit, a vapour-pressure control unit, a control box and control software written in the *LabVIEW* software (National Instruments, USA). A schematic overview of the RGVPC system is depicted in Fig. 1. In the gas-pressure control unit, as shown in Fig. 1(a), there are three types of gas bottles, 12 diaphragm sealed valves (V1–V12; Swagelok Co.), multiple solenoid valves (CKD Co.), two types of mass-flow controllers (MFC1 and MFC2; Horiba Ltd), electronic pressure gauges (G1 and G2; Baratoron capacitance manometers, MKS Instrument Inc.), a needle valve (NV1; Swagelok Co.), a turbo-molecular pump (TMP) and the control-box system containing various compact DAQs (National Instruments Co.). The gas bottles can be connected to the V4–V6 ports by

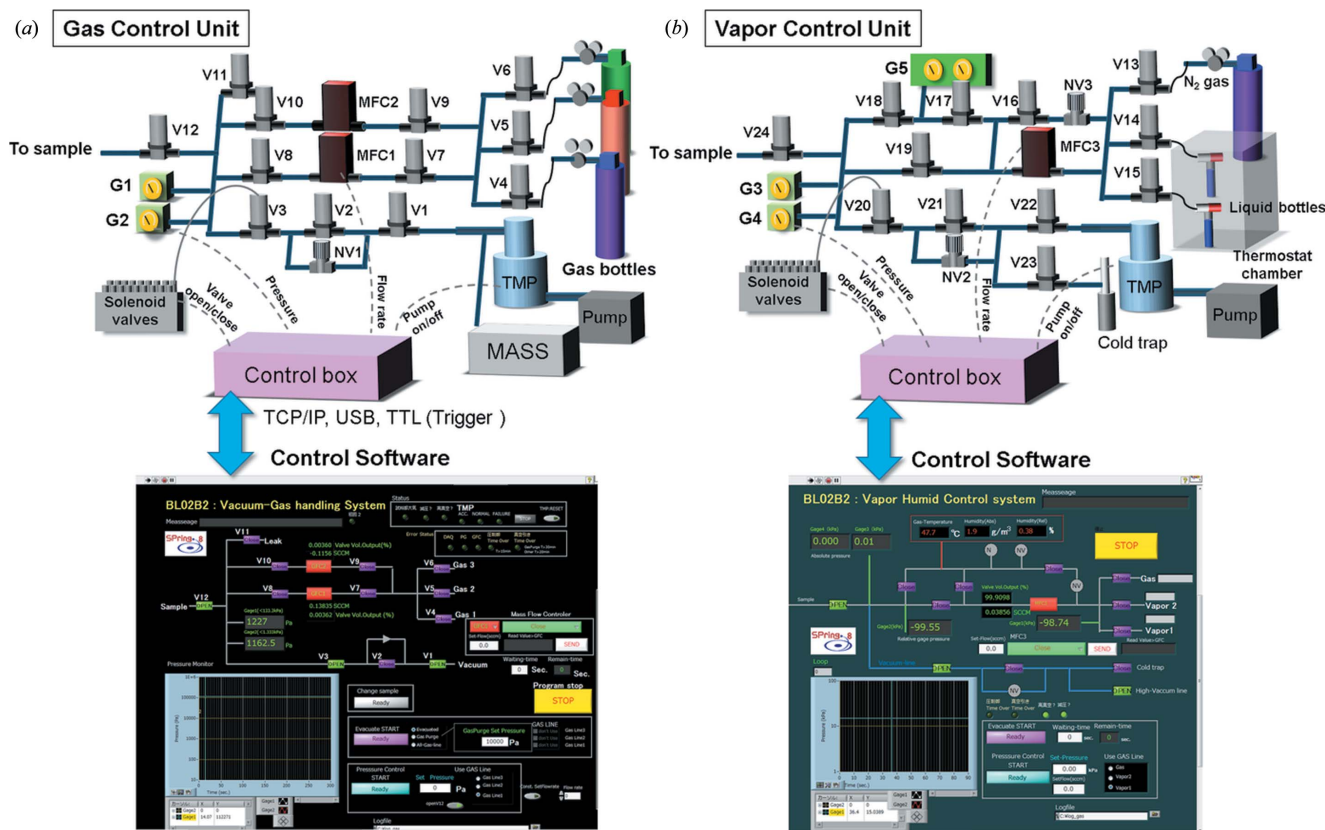


Figure 1 Schematic illustrations of the (a) gas and (b) vapour control units of the RGVPC system.

the metal fitting of Swagelok quick connects. The open/close function of the V1–V12 valves can be controlled by 0.5 MPa of air pressure. Therefore, the valves are connected to solenoid valves through 6 mm tubes. The electronic circuit in the control box can output a voltage of 5 V on the multiple solenoid valves to open the diaphragm sealed valves. When a voltage is applied to a solenoid valve, 0.5 MPa of air pressure is immediately sent to a diaphragm sealed valve. The MFC1 handles a small full scale of flow rate to accurately set the pressure, whereas MFC2 handles a large flow rate. The control software can communicate with the mass-flow controller via transmission control protocol/internet protocol (TCP/IP) communication, and it controls the flow rate (SCCM; standard cubic cm min⁻¹) and the open/close functions of the mass-flow controller. To cover the wider pressure range, we used the two types of gauges with a high precision of 0.25% reading scale (G1 with 133 kPa and G2 with 1.33 kPa full-scale ranges) to control the pressure. The effective measuring range is ~10⁻⁴ in the full scale. The electronic circuit in the control-box system can collect output voltage from the electronic gauges. Then, the control box system is connected to the developed control software on a control PC via TCP/IP and USB cables. When the gas pressure is applied to the sample, the V4 (V5 or V6), V7–V10 and V12 valves open, and the gas pressure is gradually applied by changing the flow rate of MFC1 and MFC2 via the control software. Once the pressure is set in the developed software, the flow rate is auto-adjusted by referring to the differential pressure between reading pressure gauges

and setting the pressure in the software via the control box system. For example, if the differential pressure is large, the flow rate is large. As the differential pressure decreases, the software automatically lowers the flow rate. The pressure stability is set to be within ±1 Pa for the low-pressure range (<1.3 kPa) and ±10 Pa for the high-pressure range (>1.3 kPa). This difference in pressure stability mainly comes from the difference of measurable range in the two types of gauges, and the gauge is switched at 1.3 kPa. The setting time ranges from a few seconds to minutes, depending on the differential pressure. The absolute pressure from 1 Pa to 130 kPa can be controlled. When the gas in the cell is evacuated by the pumps, the needle valve (NV1) is used to safely evacuate the gases in the capillary cell to prevent scattering of the powder sample. During the high gas pressure, the V1 and V3 valves will open and the V2 valve remains closed. In this configuration, the gas pressure is gradually decreased. Below 50 Pa, the V2 valve will open and a high-vacuum condition is then generated, and then the TMP is automatically turned on. The vacuum line is connected to the quadrupole mass spectrometer (BELMass; MicrotracBEL Co. Ltd) and the exhaust gas can be accurately monitored within 1 p.p.m.

The vapour-pressure control unit, as shown in Fig. 1(b), comprises liquid bottles, a thermostat chamber, an N₂ gas bottle, 12 diaphragm sealed valves (V13–V24), multiple solenoid valves, a mass-flow controller (MFC3), electronic pressure gauges (G3 and G4), an inline temperature humidity gauge (G5), needle valves (NV2 and NV3), a cold trap under

liquid nitrogen, a TMP and the control box. The V13–V24 valves, the solenoid valves, MFC3, G3–G4 and NV2–NV3 are the same items as with the gas-pressure control unit. Furthermore, the control unit, pumps and the TMP are shared with the gas control unit. The liquid bottles inside the thermal chamber are made of glass and can be connected to the V14 and V15 ports by an O-ring used for vacuum fitting. The thermal chamber, where the temperature can be varied between 293 and 313 K, is used to maintain the vapour pressure. When the vapour pressure is applied to the sample, V14 (or V15), V17–V19 and V24 valves open, and the vapour pressure is gradually applied by changing the flow rate of MFC3 via the control software. This control procedure is similar to the one performed in the gas-pressure control unit. However, in most cases, the control range of the vapour pressure, which depends on the solvent, is less than that of the gas pressure, therefore an MFC controller is sufficient for the vapour control unit. The vapour pressure strongly depends on the temperature; therefore, we installed the inline temperature gauge G5, which is useful for the measurement of the vapour temperature. For the evacuation processes, which are also similar to those performed in the gas-pressure control unit, first the V23 valve connected with the cold trap opens and toxic substances in the vapour lines are eliminated to avoid causing any damage to the pumps. Then the V21 and V22 valves will open to achieve a high-vacuum condition in the vapour lines. The N₂ gas and humidity gauge G5 are mainly used for cleaning the insides of the vapour lines. The NV3 and V16 valves are optional equipment to be used in the case of manual operation.

For both the gas and vapour control units of the RGVPC system, the gas lines are SUS tubes connected by 1/4-inch Swagelok metal fittings. The setting temperature of all gas and vapour lines can be up to 323 K using the electronic ribbon heater. This RGVPC system can monitor the pressure control in the closed gas and vapour lines and it does not operate with a flow of gas or vapour passing through the sample. The RGVPC system is shown in Fig. 2. The gas- and vapour-pressure control units are located in the upper and lower boxes, respectively, and the middle box is the control box. The control software is linked with another measurement program. For the time-resolved experiments, a digital delay pulse generator (DG645; Stanford Research System Co. Ltd) can be used, and the open/close operations of the valves and the reading pressure value in the RGVPC system are synchronized with the MYTHEN detector control system via the developed software. In this configuration, the frame rate reaches up to 100 Hz. Thus, the gas and vapour pressure in the capillary sample can be automatically controlled by the gas-flow rate and the opening and closing of valves through the control software.

2.3. Gas cell for capillary sample

We have developed a gas cell that can introduce gas and vapour into the capillary tube, as shown in Fig. 3. The cell is made of stainless steel and can hold a capillary funnel with a

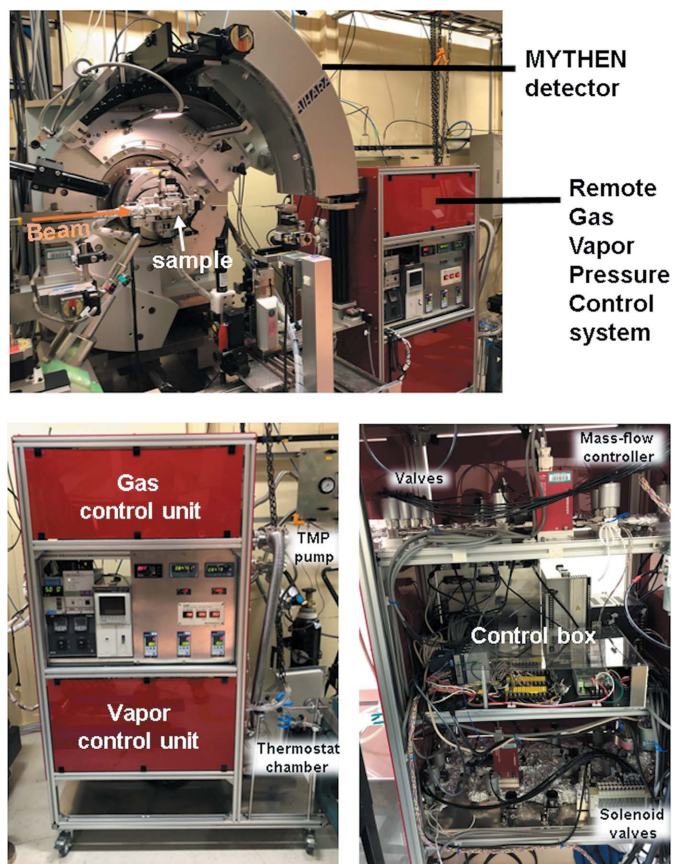


Figure 2

The powder diffractometer equipped with six one-dimensional solid-state (MYTHEN) detectors and an RGVPC system. Lower left: front view of the RGVPC system. Lower right: interior of the RGVPC system.

diameter of 3 mm. Note that a funnel of 3 mm is the standard diameter size for commercial quartz and borosilicate glass capillaries. The capillary is connected to a tapered hole on the cell side and fixed by a Viton O-ring. The hole is connected to a 1/8-inch gas line inside the cell. In this cell, by using a funnel as a connection to the gas line, any capillary with a diameter less than 3 mm can hold tightly. In addition to this cell, other types of cells designed for a 0.4 mm or 0.5 mm capillary can be

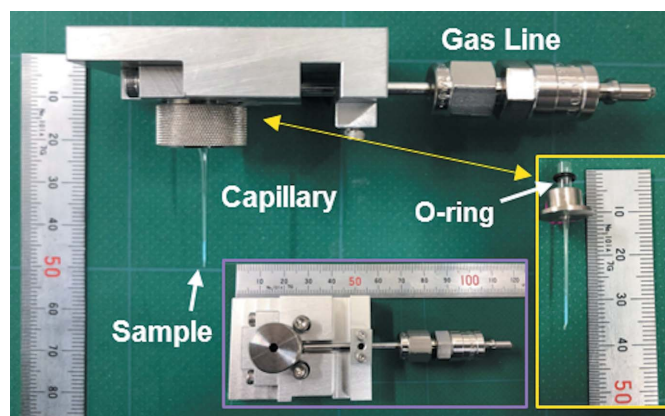


Figure 3

The gas cell developed for the capillary sample.

used. In these cells, a leak check was conducted via the Hood method by using a helium-leak detector, and the actual value was $\sim 10^{-11}$ Pa m³ s⁻¹. The gas cell can be mounted on a five-axis (Y, Z, RY, RZ, φ) sample stage on the ω axis of a powder diffractometer (Kawaguchi *et al.*, 2017). The ω axis can be oscillated from -90 to $+180^\circ$ when the mounted gas cell is connected with the gas line. In general, the oscillation of the ω axis is continuously performed during the measurements under the static condition to improve the intensity homogeneity along the Debye–Scherrer rings for Rietveld analysis. The capillary alignment can be performed by moving both the five-axis sample stage and the ω axis through the monitoring of the capillary using a CCD camera. Thus, our developed cell can be easily mounted on the capillary sample without any sealing material and the sample in the capillary can be evacuated to create a high-vacuum condition.

3. *In situ* powder diffraction under gas and vapour atmosphere

3.1. Automatic XRPD measurement under static condition

Using the RGVPC system, we can demonstrate automatic *in situ* XRPD measurement as a function of gas pressure. The sample is a MOF complex, which is a nanoporous Cu coordination polymer $[\{\text{Cu}_2(\text{pzdc})_2(\text{pyz})\}_n]$ (pzdc = pyrazine-2,3-dicarboxylate; pyz = pyrazine) (CPL-1) with a pillared layer structure containing one-dimensional nanochannels with dimensions of $4.0 \text{ \AA} \times 6.0 \text{ \AA}$ along the a axis between two-dimensional sheets and follows a typical physisorption process (isotherms of Type I). This compound can adsorb various gases (Kitaura *et al.*, 2005), and the maximum entropy/Rietveld method revealed the formation of a one-dimensional array of molecular oxygen in the nanochannels (Kitaura *et al.*, 2002). The crystal structure is shown in Figs. 4(a) and 4(b), which correspond to the structures without guest gas molecules and with adsorbed O₂ gas, respectively. Moreover, using the RGVPC system, the Rietveld refinement for the O₂ adsorption phase was performed as described in a previous study (Sugimoto *et al.*, 2017). The CPL-1 powder sample was filled into the borosilicate glass capillary, which has a diameter of 0.5 mm, and the filled capillary was loaded into the gas cell. We collected the XRPD patterns under an O₂ gas pressure, which was gradually varied using the RGVPC system. For the measurement, at first the sample was evacuated to a pressure of $\sim 10^{-5}$ Pa and the sample temperature was increased to 403 K. This is similar to the desorption treatment of some gases and H₂O in the nanochannels. Subsequently, the sample temperature was decreased to 77 K and the XRPD pattern was recorded, as shown in the data of 0 Pa in Fig. 4(c). Next, the XRPD experiments under O₂ gas pressure were carried out as follows: (i) an O₂ gas pressure (*e.g.* 3 Pa) was introduced to the sample cell, (ii) a standby time of a few minutes was held to achieve sufficient equilibrium, and (iii) a collection of XRPD patterns was obtained. The acquisition time of each XRPD pattern was 1 min. The collected XRPD patterns are shown in Fig. 4(c) and the change of O₂ gas pressure with time

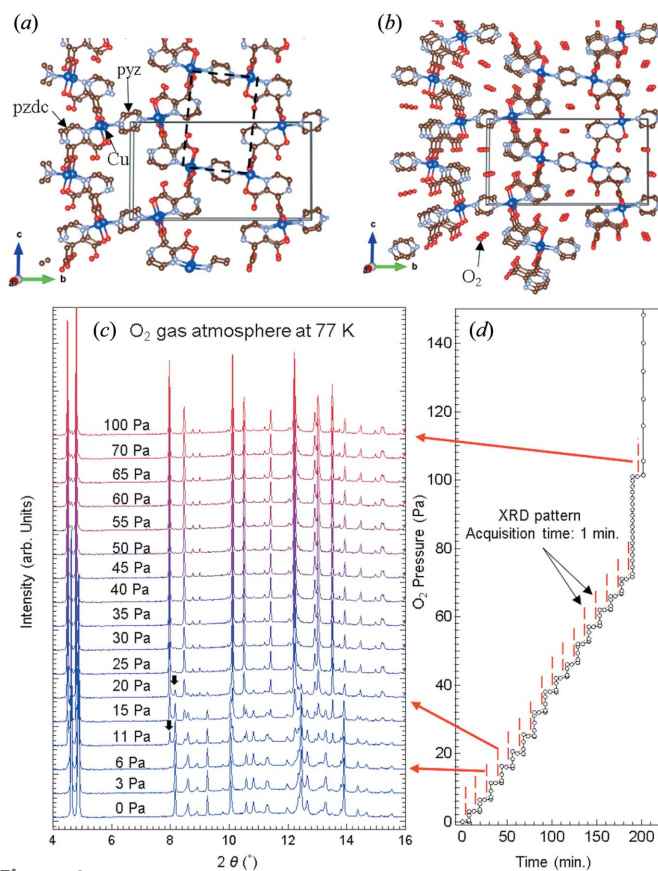


Figure 4

(a) Crystal structure of the CPL-1 sample without guest gas molecules and (b) with the adsorption of O₂ in the nanopore. The space group of both crystal structures is $P2_1/c$. The O₂ pressure dependence of (c) the XRPD patterns at 77 K and (d) time are also shown. The XRPD data were recorded by the double-step mode of MYTHEN detectors.

is shown in Fig. 4(d). In the diffraction pattern, the new peaks at 11 Pa are displayed by the arrows in Fig. 4(c). The pattern shows that structural change occurs from the desorption phase to the O₂ adsorption phase. At 25 Pa, the diffraction peaks derived from the desorption phase finally disappear. From the previous report on the measurement of O₂ adsorption isotherms (Kitaura *et al.*, 2005), CPL-1 at 77 K starts to adsorb at the 10^{-4} relative pressure range. The 10^{-4} order of relative pressure corresponds to ~ 10 Pa of absolute pressure; therefore, our measured result of structural change at 11 Pa corresponds to the previous adsorption isotherm result. Thus, the developed RGVPC system can precisely and automatically control gas pressure even at very low pressure ranges, which is otherwise difficult to control by human operation.

Fig. 5(a) shows *in situ* XRPD measurement results when methanol vapour at 298 K was used for the CPL-1 sample. Similar to the measurement under the gas atmosphere, this measurement was performed while automatically changing the vapour pressure in a stepwise manner. The pressure was changed from 0 Pa (in vacuum) to 16 kPa of methanol vapour. Note that the saturated vapour pressure of methanol at 298 K is ~ 17 kPa. As the pressure increases, the 031 Bragg peak monotonously shifts to the low diffraction angle side.

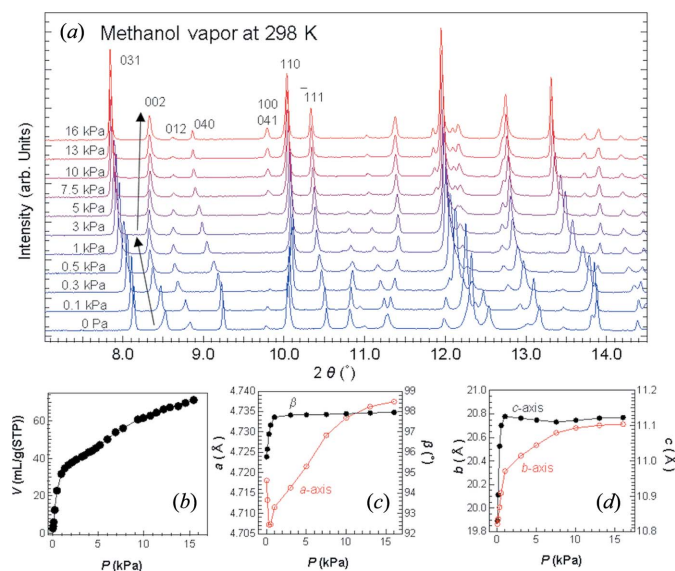


Figure 5
(a) The XRPD patterns of the CPL-1 sample at 298 K as a function of methanol vapour pressure. (b) The isothermal adsorption curve for methanol vapour at 298 K. (c) and (d) Methanol vapour pressure dependence of the lattice parameters obtained by the whole-profile fitting. STP = standard temperature and pressure.

However, the 002 Bragg peak does not show a monotonous change with increasing pressure because the peak shifts to a high angle side at 1 kPa. To investigate the behaviour of this unique change, we measured the adsorption isotherm of methanol vapour at 298 K. The measurement was performed with BELSORP-MAX II (MicrotracBEL Co. Ltd) automatic volumetric adsorption equipment. The results are shown in Fig. 5(b). It can be seen that methanol vapour is significantly adsorbed up to 1 kPa, while the amount of adsorption changes gradually at higher pressures. In addition, we calculated the lattice constants from the XRPD pattern data. Consequently, the *b* and *c* axes and β drastically increase up to 1 kPa, whereas the *a* axis decreases. At a pressure higher than 1 kPa, the *a* and *b* axes increase with increasing pressure. These structural changes are considered to correspond to the change in the amount of the adsorption of methanol. The CPL-1 sample can adsorb in some methanol molecules even at low pressure. At high pressures above 1 kPa, the framework structure of the CPL-1 sample can be changed in order to absorb more methanol molecules in narrow pores. It is expected that the details of this structural change will be clarified by conducting structural analysis in the future. From these results for the above-mentioned two cases of *in situ*

XRPD measurements under O_2 gas and methanol vapour, the RGVPC system can be useful for investigating a static crystal structure under gas and vapour atmosphere corresponding to the adsorption isotherm measurement. Finally, several structural investigations for various compounds have already been performed using the developed RGVPC system, *e.g.* a flexible MOF compound with CO_2 separation and capture function (Hiraide *et al.*, 2016, 2017); a chemo-chromism complex under vacuum and methanol vapour (Shiga *et al.*, 2018); acid responsive hydrogen-bonded organic frameworks compounds under CO_2 gas, benzene and hexane vapour (Hisaki *et al.*, 2018, 2019); and hydrogen-storage alloys under H_2 and D_2 gases (Dekura *et al.*, 2018).

3.2. Time-resolved XRPD experiment under gas pressure

In order to observe the fast and dynamic structural change for gas pressure, we developed two types of measurement technique: the sweeping pressure mode and the gas-shot mode. For the former, fast diffraction measurements with equal interval are performed continuously under changing pressure. Fig. 6 represents a part of the 1200 data points of the XRPD patterns of the CPL-1 sample under vacuum for various O_2 pressure values. The O_2 gas pressure was changed by flowing O_2 gas at a rate of 1 and 0.5 SCCM for 110 K and 97 K, respectively. The acquisition time for each diffraction dataset was 0.3 s, and the wait time was set to 0.05 s between each dataset to safely synchronize with acquisition of the diffraction data and the pressure control. The obtained data were converted into an intensity map with 2θ versus time using the software, which was developed using *LabVIEW* and *Python*, for the purpose of clarification. In Fig. 6, the transition

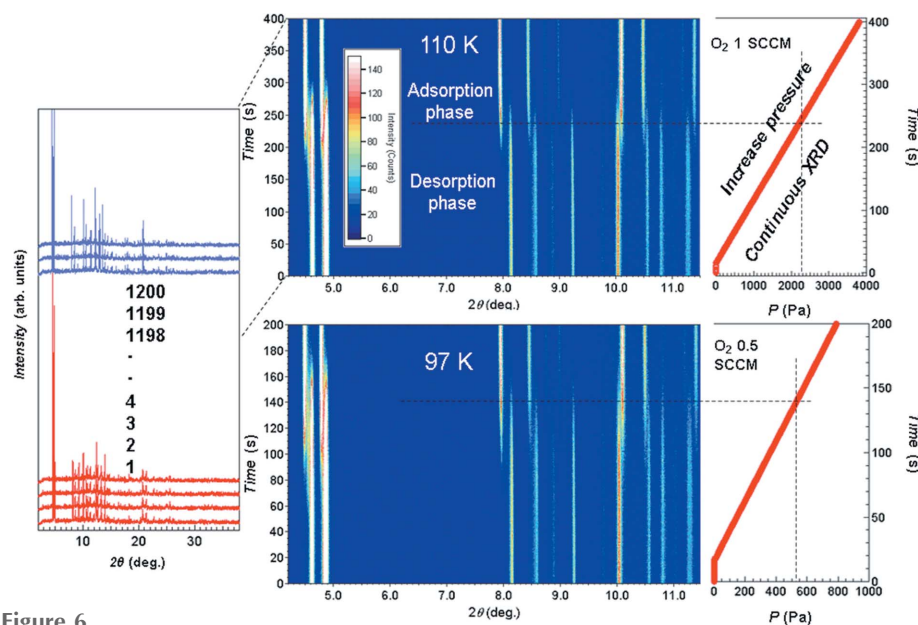


Figure 6
Time-resolved XRPD data under O_2 atmosphere at 97 K and 110 K for the CPL-1 sample. The data were recorded in the sweeping pressure mode. The one-dimensional XRPD data (left-hand column), intensity map of the XRPD data (middle column) and the time dependence of the O_2 gas pressure (right-hand column) are shown. The O_2 flow rate was 1 SCCM and 0.5 SCCM for 110 K and 97 K, respectively.

from desorption phase to adsorption phase is clearly observed at 250 s for 110 K and 140 s for 97 K. It turns out that this transition can essentially be interpreted as the two phases coexisting, and the gas pressure for the transition (gating pressure) is roughly estimated for the data at each temperature. The gate-opening pressure is 2.5 kPa for 110 K and 0.5 kPa for 97 K.

Fig. 7 shows the diffraction patterns in the adsorption processes of Ar and CH₄ gases. In the Ar gas adsorption process, the transition from desorption phase to adsorption phase occurs at ~3 kPa after 100 s. The behaviour of the phase transition in the case of Ar gas adsorption is similar to that of the O₂ gas adsorption, but the gate-opening pressure is several times more than in the case of O₂ adsorption. In contrast to this, the structural changes in the CH₄ gas adsorption process show the appearance of the intermediate phase around 4.8° in 2θ in addition to the desorption and adsorption phases. This phase originates from a metastable phase existing in the adsorption process of CH₄ gas (Kitaura *et al.*, 2005). The structural refinement of this phase was performed (Kitaura *et al.*, 2005) and this intermediate phase adsorbs 0.5 molecules of CH₄ gas per Cu ion and is attributed to the fitting of guest molecules resulting from the framework flexibility of CPL-1. Interestingly, the peak position gradually moves with the increase in the pressure from 1 to 4 kPa. This shift in peak position indicates that various structures, which in the adsorption structure change from a metastable phase with a low packing density to a stable phase with a saturated packing density, exist for the pressure in the metastable phase. Therefore, notably, the gate-opening pressure and the transition from desorption phase to adsorption phase largely depend on the gas species. The adsorption structure and the transition might be affected by the size and shape of the gas molecules. For example, the molecular size of Ar (3.405 Å) is larger than that of O₂ (2.930 Å) (Webster *et al.*, 1998). The size of an Ar molecule is nearly the same as the pore size (4.0 Å × 6.0 Å) of CPL-1. In this case, the gate-opening pressure of Ar adsorption is higher than that of O₂ adsorption in order to overcome the potential barriers in the nanopores. Thus, the RGVP system can be advantageous for visualizing the overall structural change in adsorption or desorption

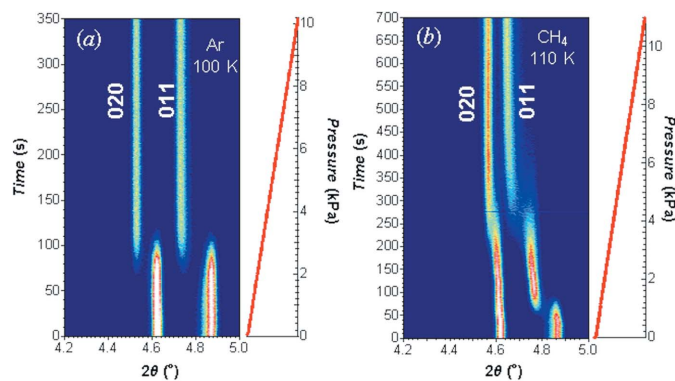


Figure 7 Time dependence of the XRPD intensity map under (a) Ar gas at 100 K and (b) CH₄ gas at 110 K for the CPL-1 sample.

processes and can speedily acquire information on the structural phases of various gas pressures and gas species.

Using the gas-shot mode, we conducted time-resolved XRPD measurements for the CPL-1 sample under the O₂ gas adsorption process, and the time dependence of XRPD intensity is shown in Fig. 8(a). This mode immediately applies a fixed amount of gas to a sample at a determined time. The XRPD patterns were continuously obtained by exposing the sample for 0.3 s at regular intervals of 50 ms. After 17.5 s of initiating the XRPD measurements, the O₂ gas of 3 kPa in the RGVP system was automatically introduced into the sample in a glass capillary by opening the diaphragm sealed valve of a nearby gas cell. Here, we define the time of opening the valve as t_{gate} . Fig. 8(b) shows the time dependence of the O₂ pressure. Notably, the pressure reached 3 kPa within 1 s after t_{gate} . Fig. 8(c) shows the time dependence of the intensity of the 031 Bragg peak. The peak intensity of the desorption phase is observed to decrease and that of the adsorption phase is observed to gradually increase. Thus, the CPL-1 sample immediately absorbs the O₂ gas, and the desorption and adsorption phases coexist at 10 s after t_{gate} . In order to study the change of the framework structure of the CPL-1 sample during this adsorption process, whole-pattern fitting based on the Le Bail method was performed for each time-resolved XRPD data. The fittings were performed using JANA2006

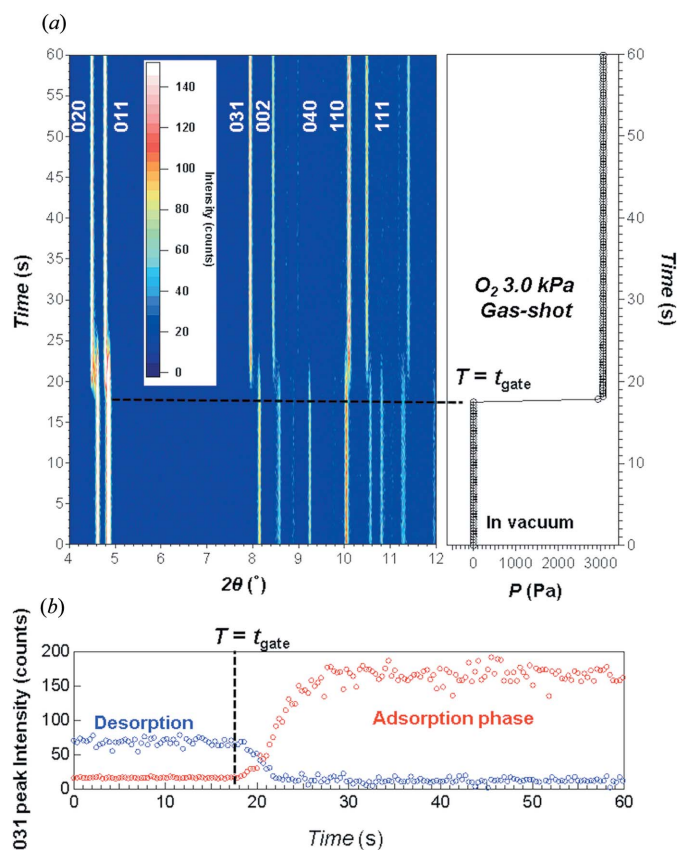


Figure 8 (a) Time-resolved XRPD intensity map at 97 K using the gas-shot mode. (b) Time dependence of the O₂ pressure and the 031 Bragg intensity. The O₂ is introduced to the CPL-1 sample at t_{gate} .

software (Petříček *et al.*, 2014). The obtained lattice parameters and volume are shown in Figs. 9(a)–9(c). The change of lattice parameter is exceedingly small, *i.e.* less than 0.01 Å, and therefore a high-resolution XRPD technique is necessary for this observation. The volume and *b* axis in the desorption and adsorption phases gradually increases after t_{gate} . On the other hand, it was observed that the *a* axis in the adsorption phase shows a kink at 22 s. The origin of these behaviours could not be clearly understood in this study but the time-resolved XRPD results indicate that the increasing volume in the desorption phase after t_{gate} means that there are intermediate structures in which some amount of the O₂ molecules are adsorbed in empty nanopores. In the saturated adsorption phase, O₂ molecules in the nanopores are slightly canted from the *a*-axis direction which corresponds to the direction of the nanopore channel. The characteristic behaviour of the *a* axis may mean that the O₂ molecules are temporarily adsorbed in the unstable potential in the pores, *e.g.* the molecules are aligned parallel to the *a*-axis direction, and the molecules are rearranged to a stable position in the nanopores. In this study, the capillary sample was not rotated for the time-resolved experiments but the uniform intensity of the Debye–Scherrer ring of the CPL-1 sample was confirmed by the two-dimensional detector. However, to improve the powder average statistics for performing the Rietveld refinement, a further development of the gas cell with a high-speed rotation

mechanism is necessary for advanced time-resolved XRPD experiments. In the future, in order to reveal the intermediate crystal structures and to elucidate their origin, it is necessary to perform the structural analysis using both Rietveld refinement and pair distribution function analysis for the time-resolved XRPD data in a temporal resolution of milliseconds or less.

To investigate the kinetics of the phase changes, the data obtained were analyzed using kinetic methods such as the Kolmogorov–Johnson–Mehl–Avrami (KJMA) equation (Avrami, 1939; Krüger, 1993). The equation is as follows,

$$V = 1 - \exp(-Kt^n),$$

where V is the fraction transformed at time t , K is the rate constant and n is related to the number of dimensions in which the transition occurs. We apply this equation to the time-resolved data at 97 K after t_{gate} . Here, the fraction of adsorption phase was calculated by normalizing the average intensity of the 031 Bragg reflection in the adsorption phase, and the time t_{gate} was defined as $t = 0$. We also collected data under various gas-shot pressures. The results are shown in Fig. 9(d). The solid lines represent the fitting of the KJMA equation. The obtained rate constant K is drawn in Fig. 9(e) as a function of applying gas pressure. The obtained n values were ~ 1.3 – 1.5 for all data. This result indicates the quasi-one-dimensional growth of adsorption phase for the CPL-1 sample, corresponding to a crystal structure with a one-dimensional nanopore channel. The K values increase linearly with the pressure applied. This result suggests that the rate constant depends on the pressure of O₂. It is expected that the temperature is strongly related to the speed of the adsorption process because the gate-opening pressure was changed by the temperature. Extrapolating to the K values, as shown in Fig. 9(e), allows the end time of the transition from desorption to adsorption to be obtained. For example, when an O₂ pressure of 20 kPa is applied to the CPL-1 sample at 97 K, 94% of the transition is completed within 2 s. Thus, this approach can be used even if the crystal structure is unknown or very complicated and will help in discussion of the nature of the transition between adsorption and desorption phases and the speed of the adsorption mechanism in pores. Now, the time-resolved XRPD experiments using the RGVPC system have been conducted for various materials, and the detailed results of the KJMA analysis for the MOF compound ELM-11, which has a high-speed responsiveness to the gas feed, will be reported in the near future (Hiraide *et al.*, to be submitted). We believe that the experimental evidence obtained by the RGVPC system not only improves the understanding of the adsorption mechanism via crystal-structure analysis for time-resolved data but also facilitates the development of gas adsorption/separation materials and applications for pressure/vacuum-swing adsorptions.

4. Conclusions

This study reported the design and performance of a new RGVPC system synchronized with the continuous acquisition

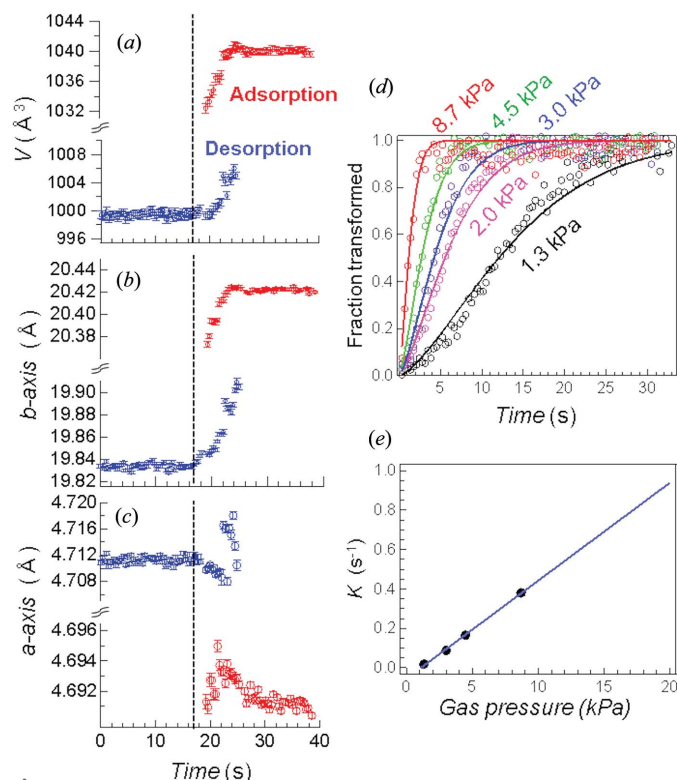


Figure 9

Time dependence of (a) the volume, and (b) and (c) the lattice parameters obtained by the whole-pattern fitting to the time-resolved XRPD data recorded by the gas-shot mode. (d) The fractions of adsorption phase transformed as a function of time. The solid lines were calculated by the KJMA fitting. (e) O₂ gas pressure dependence of the rate constant obtained by the KJMA fitting.

of high-resolution XRPD measurement data at a beamline of SPring-8. Using these apparatuses, *in situ* XRPD measurements under gas and vapour pressure were performed automatically even at a very low pressure range. From the results of the *in situ* XRPD measurements of the CPL-1 sample, the RGVPC system demonstrated a capability to investigate a static crystal structure under gas and vapour atmospheres corresponding to an adsorption isotherm measurement. We developed two types of techniques for time-resolved measurement under gas pressure: the sweeping-pressure mode and the gas-shot mode. The latter is a method of immediately applying a fixed amount of gas to a sample. In the sweeping-pressure mode, the overall picture of structural changes in the adsorption or desorption processes was easily visualized for the CPL-1 sample; this mode can lead to the collection of structural phase diagram data for gas pressures and species. In the experiments for the CPL-1 sample using the gas-shot mode, we observed the structural changes from the desorption to adsorption phases within 10 s of applying a gas pressure of 3 kPa. The lattice parameters were obtained by whole-pattern fitting for the time-resolved data. The lattice parameters showed characteristic change for the gas pressure; it was very small, *i.e.* less than 0.01 Å. Further detailed crystallographic investigations will be reported in the future. The data obtained were subsequently analyzed using the KJMA equation to investigate the kinetics of the phase changes. The rate constant and mechanism of nuclei formation for the adsorption phase, as obtained from this analysis, may help us to discuss the adsorption mechanism. To fully reveal a snapshot of crystal structures under gas adsorption processes at a temporal resolution of milliseconds, it would be necessary to use a new detector system and further increase the photon flux, which is enough to ensure that the sample will not be damaged by X-rays. The desirable X-ray detectors have small pixel sizes of less than 100 µm, a high sensitivity for high-energy X-rays, a high temporal resolution (an order of less than a millisecond) and a wide measurable diffraction-angle range without the module gap. Furthermore, an approach from data science such as Bayesian inference will also be important for time-resolved data with poor counting statistics. In the near future, we will attempt to install and develop these measurement systems. Finally, our developed RGVPC apparatus could contribute to *in situ* and/or time-resolved measurements for studying chemical-reaction processes, gas storage/separation and catalytic reactions in various functional materials.

Acknowledgements

The synchrotron radiation experiments were performed at beamline BL02B2 of SPring-8 with the approval of the Japan Synchrotron Radiation Research Institute (JASRI) (Proposal Nos. 2016B1959, 2017A1856, 2018A1192, 2018B2098 and 2019A2052). The authors thank Professor R. Matsuda and Professor S. Kitagawa for their assistance with the preparation of the CPL-1 sample. The authors also thank MicrotracBEL Co. Ltd for their help with the manufacture of the gas cells.

Funding information

This research was supported by KAKENHI Grant No. (18K18310) from the Japan Society for the Promotion of Science (JSPS).

References

- Avrami, M. (1939). *J. Chem. Phys.* **7**, 1103–1112.
- Bergamaschi, A., Cervellino, A., Dinapoli, R., Gozzo, F., Henrich, B., Johnson, I., Kraft, P., Mozzanica, A., Schmitt, B. & Shi, X. (2010). *J. Synchrotron Rad.* **17**, 653–668.
- Brunelli, M. & Fitch, A. N. (2003). *J. Synchrotron Rad.* **10**, 337–339.
- Carrington, E. J., Vitórica-Yrezábal, I. J. & Brammer, L. (2014). *Acta Cryst.* **B70**, 404–422.
- Cho, S. H., Miyasaka, K., Kim, H., Kubota, Y., Takata, M., Kitagawa, S., Ryoo, R. & Terasaki, O. (2012). *J. Phys. Chem. C*, **116**, 25300–25308.
- Dekura, S., Kobayashi, H., Ikeda, R., Maesato, M., Yoshino, H., Ohba, M., Ishimoto, T., Kawaguchi, S., Kubota, Y., Yoshioka, S., Matsumura, S., Sugiyama, T. & Kitagawa, H. (2018). *Angew. Chem. Int. Ed.* **57**, 9823–9827.
- Haverkamp, R. G. & Wallwork, K. S. (2009). *J. Synchrotron Rad.* **16**, 849–856.
- Hill, A. H. (2013). *J. Appl. Cryst.* **46**, 570–572.
- Hiraide, S., Tanaka, H., Ishikawa, N. & Miyahara, M. T. (2017). *Appl. Mater. Interfaces*, **9**, 41066–41077.
- Hiraide, S., Tanaka, H. & Miyahara, M. T. (2016). *Dalton Trans.* **45**, 4193–4202.
- Hisaki, I., Nakagawa, S., Suzuki, Y. & Tohnai, N. (2018). *Chem. Lett.* **47**, 1143–1146.
- Hisaki, I., Suzuki, Y., Gomez, E., Ji, Q., Tohnai, N., Nakamura, T. & Douhal, A. (2019). *J. Am. Chem. Soc.* **141**, 2111–2121.
- Jensen, T. R., Nielsen, T. K., Filinchuk, Y., Jørgensen, J.-E., Cerenius, Y., Gray, E. M. & Webb, C. J. (2010). *J. Appl. Cryst.* **43**, 1456–1463.
- Kawaguchi, S., Takemoto, M., Osaka, K., Nishibori, E., Moriyoshi, C., Kubota, Y., Kuroiwa, Y. & Sugimoto, K. (2017). *Rev. Sci. Instrum.* **88**, 085111.
- Kitaura, R., Kitagawa, S., Kubota, Y., Kobayashi, T., Kindo, K., Mita, Y., Matsuo, A., Kobayashi, M., Chang, H., Ozawa, T., Suzuki, M., Sakata, M. & Takata, M. (2002). *Science*, **298**, 2358–2361.
- Kitaura, R., Matsuda, R., Kubota, Y., Kitagawa, S., Takata, M., Kobayashi, C. T. & Suzuki, M. (2005). *J. Phys. Chem. B*, **109**, 23378–23385.
- Krüger, P. (1993). *J. Phys. Chem. Solids*, **54**, 1549–1555.
- Kubota, Y., Takata, M., Kobayashi, T. & Kitagawa, S. (2007). *Coord. Chem. Rev.* **251**, 2510–2521.
- Norby, P. (1997). *J. Am. Chem. Soc.* **119**, 5215–5221.
- Petříček, V., Dušek, M. & Palatinus, L. (2014). *Z. Kristallogr.* **229**, 345.
- Schmitt, B., Brönnimann, C., Eikenberry, E. F., Gozzo, F., Hörmann, C., Horisberger, R. & Patterson, B. (2003). *Nucl. Instrum. Methods Phys. Res. A*, **501**, 267–272.
- Shiga, M., Kawaguchi, S., Fujibayashi, M., Nishihara, S., Inoue, K., Akutagawa, T., Noro, S., Nakamura, T. & Tsunashima, R. (2018). *Dalton Trans.* **47**, 7656–7662.
- Sugimoto, K., Kawaguchi, S. & Takemoto, M. (2017). *Powder Diffr.* **32**, S19–S26.
- Thompson, S. P., Parker, J. E., Marchal, J., Potter, J., Birt, A., Yuan, F., Fearn, R. D., Lennie, A. R., Street, S. R. & Tang, C. C. (2011). *J. Synchrotron Rad.* **18**, 637–648.
- Thompson, S. P., Parker, J. E., Potter, J., Hill, T. P., Birt, A., Cobb, T. M., Yuan, F. & Tang, C. C. (2009). *Rev. Sci. Instrum.* **80**, 075107.
- Wang, J., Toby, B. H., Lee, P. L., Ribaud, L., Antao, S. M., Kurtz, C., Ramanathan, M., Von Dreele, R. B. & Beno, M. A. (2008). *Rev. Sci. Instrum.* **79**, 085105.
- Webster, C. E., Drago, R. D. & Zerner, M. C. (1998). *J. Am. Chem. Soc.* **120**, 5509–5516.